Materials Advances

ROYAL SOCIETY OF CHEMISTRY

PAPER

View Article Online
View Journal | View Issue

Cite this: *Mater. Adv.*, 2021, 2, 3629

An ultrathin and compact electron transport layer made from novel water-dispersed Fe_3O_4 nanoparticles to accomplish UV-stable perovskite solar cells†

Song Fang,‡[a] Bo Chen,‡[a] Bangkai Gu,[a] Linxing Meng,[a] Hao Lu *[a] and Chang Ming Li *[abcd]

Received 31st December 2020,
Accepted 6th April 2021

DOI: 10.1039/d0ma01027h

rsc.li/materials-advances

UV induced decomposition of perovskite material is one of the main factors to severely destroy perovskite solar cells for instability. Here we report a UV stable perovskite solar cell with an Fe_2O_3 electron transport layer (ETL) made by spin-coating water dispersed Fe_3O_4 nanoparticles. Devices with Fe_2O_3 ETLs prepared from 10 nm Fe_3O_4 nanoparticles show nearly no decrease of photoelectric conversion efficiency (PCE) upon continuous exposure to very high UV light irradiation (300 W Xe lamp) for 10 hours in contrast to the TiO_2 ETL based samples with more than 30% reduction of PCE, and their PCE (14.33) is also much superior to those of devices with Fe_2O_3 ETLs made conventionally from $FeCl_3$ solution (7.7%). Through the study of Fe_2O_3 thin film prepared perovskite solar cells, it is found that compact, high transmittance, low leakage and low transmission impedance devices can be obtained by using an appropriate size of Fe_3O_4 nanoparticles. Our major findings are expected to provide a guide to design UV-protected compact electron transport layers for UV-stable perovskite solar cells.

Introduction

Solar cells are a widely studied clean energy source.[1–6] Perovskite solar cells have been one of the most important solar cells for sustainable clean energy in recent years,[7–10] and normally consist of five parts: conductive glass such as F-doped tin oxide (FTO) and In-doped tin oxide (ITO), an electron transport layer (ETL), a light absorbing layer that is also called the perovskite layer, a hole transport layer like Spiro-OMeTAD and a black electrode like gold and silver.[11–13] The photoelectric conversion efficiency (PCE) of this type of solar cell has increased from 3.8% to more than 25% within about one decade.[14–17] Although the PCE of perovskite solar cells is high, their stability is still not good enough for practical applications. The first reason is the corrosion of solar cells by water and oxygen in air, which could be solved by well packaging the solar cells or by treating the outer surface of the solar cells against water in air to directly come into contact with the perovskite layer.[18,19] The second reason is the decomposition of the perovskite layer caused by the rise of temperature during the use of the solar cells. In this case, we can use perovskite materials with better thermal stability or two-dimensional perovskite materials instead of low-thermally stable perovskite materials to achieve stable operation of devices.[20–22] Thirdly, the ultraviolet part of sunlight reacts with the ETLs such as TiO_2 to decompose the perovskite layer, for which it is highly demanded to study the use of the ultraviolet protection layer for improving the stability.[23,24]

Iron oxide (Fe_2O_3) is an n-type semiconductor with visible light absorption, which has a suitable energy band position, very good chemical stability and low price.[25–27] Also, it can be considered that the ultraviolet instability of perovskite materials is mainly due to the photocatalytic reaction between the electron transport layer materials and the perovskite layer, which destroys the perovskite layer and reduces the stability of the device. Therefore, Fe_2O_3 has been widely used as a UV-stable ETL in perovskite solar cells. Wang *et al.* reported the spin-coating method to prepare an Fe_2O_3 thin film as an ETL in perovskite solar cells with 10.7% PCE[28] with stability over 30 days upon exposure to ambient air. Fe_2O_3 based devices show good stability performance but their PCE is still low. Guo *et al.* used a Ni doped

[a] *Institute of Materials Science & Devices, School of Materials Science and Engineering, Suzhou University of Science and Technology, Suzhou, 215009, China. E-mail: haolu@usts.edu.cn*
[b] *Jiangsu Key Laboratory of Micro and Nano Heat Fluid Flow Technology and Energy Application, School of Environmental Science and Engineering, Suzhou University of Science and Technology, Suzhou 215009, China*
[c] *Institute of Advanced Cross-Field Science and College of Life Science, Qingdao University, Qingdao 200671, P. R. China*
[d] *Institute for Clean Energy & Advanced Materials, Southwest University, Chongqing, 400715, P. R. China. E-mail: ecmli@swu.edu.cn*

† Electronic supplementary information (ESI) available. See DOI: 10.1039/d0ma01027h

‡ These authors contributed equally to this work.

Fe_2O_3 thin film as an ETL in perovskite solar cells, in which the Ni dopant could effectively improve the conductivity.[29] The PCE of Ni–Fe_2O_3 ETL based devices reaches 14.2% with a 154% increase compared to that without the Fe_2O_3 doped devices. High PCE and stable perovskite solar cells can be obtained by preparing high-quality Fe_2O_3 thin films, but it is difficult due to the low electronic conductivity and crystallinity of Fe_2O_3. It has been reported to be an effective approach to prepare SnO_2 and NiO_x thin films by firstly preparing nanoparticles and then assembling them for a thin film.[30–33] At the same time, nanocomposites also have unique properties and wide applications.[34,35]

Here, we made UV-stable perovskite solar cells with Fe_2O_3 films by spin-coating adjustable Fe_3O_4 water-dispersed nanoparticles. Water-dispersed Fe_3O_4 nanoparticles with different sizes can be prepared by magnetic field control, and Fe_2O_3 films can be obtained by the post annealing process. The thickness of Fe_2O_3 films can be controlled by the spin coating speed, different sizes of Fe_3O_4 nanoparticles and concentration of solution. The best device with nanoparticle prepared solar cells has a PCE of 14.3% which is 185% higher than the device using Fe_2O_3 ETLs by $FeCl_3$ solution with 7.7% PCE. Perovskite solar cells with Fe_2O_3 films could retain less than 5% decreased PCE upon continuous 300 W Xe lamp exposure for 10 hours while the TiO_2 prepared samples show 30% reduction in PCE. The mechanism for excellent performance has been studied by investigating the cell parameters including the size and concentration of Fe_3O_4 nanoparticles, thickness and annealing temperature of the layer, transmittance and absorbance of the used light, leakage current and charge transfer and recombination processes of solar cells. Our work provides an easy, promising and environmentally friendly method to prepare UV-stable Fe_2O_3 layers to increase the performance of perovskite solar cells.

Experimental section

Preparation of Fe_2O_3 and TiO_2 films

Fe_2O_3 films with Fe_3O_4 nanoparticles were prepared by spin-coating water-dispersed Fe_3O_4 nanoparticles with different spin speeds from 3000 to 6000 rpm, different concentrations from 4 mg ml^{-1} to 18 mg ml^{-1} and different sizes from 5 nm to 20 nm. The as-prepared structures were annealed at different temperatures from 450 °C to 600 °C. The Fe_2O_3 film with $FeCl_3$ solution was prepared by dissolving $FeCl_3{\cdot}6H_2O$ (Alfa Aesar, 97%) in DI water with a concentration of 0.075 M. The as-prepared solution was dropped onto the ITO layer with 4000 rpm for 30 s followed by annealing at 550 °C for 120 min in air. The TiO_2 ETL was prepared by spin-coating 0.15 g ml^{-1} titanium isopropoxide (Alfa Aesar, 95%) ethanol solution with 3000 rpm for 40 s, and then annealed at 500 °C for 120 min.

Fabrication of perovskite solar cells

Perovskite solar cells were fabricated by a modified two step approach.[36] Firstly, a PbI_2 solution with 600 mg ml^{-1} in DMF was dropped on the Fe_2O_3 substrate with 3000 rpm for 30 s. After spinning PbI_2 for 10 seconds, 30 ml of 60 mg ml^{-1} FAI, 6 mg ml^{-1} MABr and 6 mg ml^{-1} MACl solution was dropped on the substrate rapidly, and the color of the substrate changed from yellow to brown at the same time. Then the substrate was placed on a hot plate at 150 °C for 10 min in air. The HTL was prepared by spin-coating 72.3 mg ml^{-1} of Spiro-OMeTAD solution in acetonitrile at 2000 rpm for 40 s. After the spin-coating of the HTL, devices were oxidized in air for 36 h. Finally, a 100 nm thick Au electrode was deposited by thermal evaporation with a shadow mask (0.15 cm^2 active area).

Characterization and measurement

The morphologies of the samples were characterized using transmission electron microscopy (JEOL, 2100F) and field-emission scanning electron microscopy (Hitachi, SU8010). The films were also investigated by X-ray diffractometry (Bruker, D8 Advance), X-ray photoelectron spectroscopy (Thermo, Escalab 250Xi) and Raman spectroscopy (Horiba, Labram Hr Evolution). The photoluminescence and time-resolved photoluminescence were tested with a 530 nm laser (Edinburgh Instruments, LP320). The absorbance measurement was tested using UV-2600 (Shimadzu). The photovoltaic parameters of solar cells were measured under Newport solar simulator AM 1.5G irradiation (100 mW cm^{-2}) with a Keithley 2400 Source Meter, and IPCE curves were characterized using a Zolix system. Electrochemical Impedance Spectroscopy (EIS and *M–S* plots were measured under AM 1.5G light conditions with an alternative signal amplitude of 10 mV and in the frequency range of 0.1 Hz–40 kHz (Autolab PGSTAT 302N) in a glove box.

Results and discussion

A high-quality nanoparticle film requires very good size uniformity, and thereby we use a magnetic field control method to prepare Fe_3O_4 nanoparticles to effectively avoid agglomerations of crystal nuclei in the growth process by adjusting the magnetic field while tuning the reaction time for differently sized nanoparticles. Besides, growing in aqueous solution is also a very important condition. Considering that we will apply the nanoparticles in green energy solar cells, we hope to minimize the use of environmentally unfriendly solutions. Fig. 1 shows the transmission electron microscopy (TEM) and high-resolution transmission electron microscopy (HRTEM) images of Fe_3O_4 nanoparticles with different sizes. Fig. 1a shows the TEM image of 5 nm Fe_3O_4 nanoparticles, in which nanoparticles have a very uniform size. Fig. 1b and c show the TEM images of 10 nm and 20 nm Fe_3O_4 nanoparticles, in which nanoparticles have the same morphology, uniform size and good dispersion. Fig. S1 (ESI†) shows the images of solution with the same 6 mg ml^{-1} concentration (measured by Fe). The different size nanoparticles in the same concentration have different colors which may due to the size effect in light transfer. Fig. 1d shows the HRTEM image of Fe_3O_4

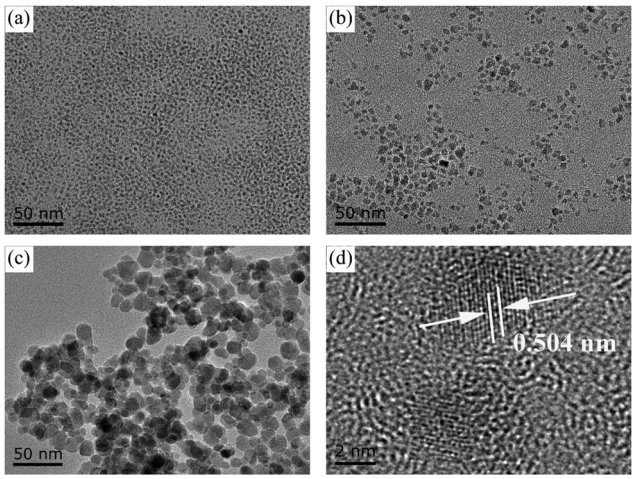

Fig. 1 TEM images of Fe_3O_4 nanoparticles: (a) 5 nm, (b) 10 nm and (c) 20 nm. (d) HRTEM of 5 nm Fe_3O_4 nanoparticles.

nanoparticles, from which we can see a high-quality crystal with 2.52 Å in the (311) plane and that the surface of nanoparticles is clean which is good for carrier transport.[37,38]

Scanning electron microscopy (SEM) was used here to show the morphology of the as-prepared films on the In-doped tin oxide (ITO) structure. Fig. 2a shows the schematic of different Fe_2O_3 films which were prepared by nanoparticles and $FeCl_3$ solution. Due to the excellent hydrophilic properties of water dispersed nanoparticles, the films can be self-assembled on the ITO surface, and high-quality iron oxide films can be obtained because of the small change in the crystal structure in the annealing process. For the films prepared using $FeCl_3$ solution, the spin coated $FeCl_3$ film has a good density, but in the post annealing process, the crystallization process of iron oxide will cause the formation of a large number of holes in the original compact film. Fig. 2b shows the morphology of ITO glass without any treatment, which has clear surface and acicular grains. Fig. 2c shows the morphology of ITO glass with the Fe_2O_3 film which is prepared by spin-coating 10 nm Fe_3O_4 nanoparticles with a concentration of 6 mg ml^{-1} (measured by Fe). After spin-coating the Fe_3O_4 nanoparticles and annealing to form the Fe_2O_3 film, the morphology of the substrate surface shows no obvious change in comparison to that of ITO glass, and almost no pin-hole could be found. The morphologies of devices with 5 nm and 20 nm Fe_3O_4 nanoparticles are shown in Fig. S2 (ESI†), and are similar to the morphology of 10 nm devices with quite a good compact surface, but a small number of particles accumulated on the surface. Fig. 2d shows the morphology of the Fe_2O_3 film which is prepared by spin-coating $FeCl_3$ solution and annealing, and we can see that the film is more like a network structure than a compact film. These holes in the mesh may lead to direct contact between the perovskite layer and ITO glass, which will damage the transport process of the carriers of the device. Generally speaking, the local network structure has better hydrophilicity, which is conducive to the diffusion of liquid on the surface, so we performed a contact angle test and is shown in Fig. S3 (ESI†).[39,40] It could be seen from the test that the compact film prepared by 10 nm particles has a similar contact angle to the network film prepared using $FeCl_3$ solution which means that they have similar hydrophilicity. Raman spectra were used here to give more information on samples before and after annealing. From Fig. 2e, we can see that all curves have three characteristic peaks of Fe_2O_3 at 247, 288 and 634 cm^{-1}, and the curve of the sample after annealing has a stronger peak at 634 cm^{-1} which indicates that the sample has better crystallization properties of Fe_2O_3.[41–43] Fig. S4 (ESI†) shows the X-ray diffraction (XRD) pattern of the prepared sample with Fe_3O_4 nanoparticles from which we can see that there is an Fe_3O_4 peak nearly at 30° of (220) (JCPDS No. 72-2303) and after annealing there is no obvious peaks of Fe_3O_4 which means that Fe_3O_4 was converted into Fe_2O_3 by the annealing process. The bulge at low angle is caused by the plastic sample table. The absorbance spectrum (Fig. S5, ESI†) shows that devices prepared by different ways have excellent optical transmittance performance and relatively small amounts of absorption at 400 to 600 nm. Through the above discussion, the films prepared with nanoparticles are found to have very good compactness and light transmittance performance. Fig. 3 shows the schematic of the charge transport mechanism of different Fe_2O_3 layers. In the compact Fe_2O_3 layer which was prepared using Fe_3O_4 nanoparticles, carriers can be very well transmitted and separated. But, in $FeCl_3$ prepared Fe_2O_3 layers, the perovskite layer may be in direct contact with the ITO layer because of the existence of a large number of holes, carriers in the transmission process is easy to recombine.

Fig. 4 shows the typical SEM images of the perovskite layer on Fe_2O_3 films with Fe_3O_4 nanoparticles. Fig. 4a shows the top-view SEM image of the perovskite layer on the 10 nm Fe_3O_4 nanoparticle prepared Fe_3O_3 ETL, from which we can see that the perovskite has very good compactness, and the perovskite grain size is large. The perovskite layer on different nanoparticles and the $FeCl_3$ prepared Fe_3O_3 ETL can be seen in Fig. S6 (ESI†). All of them show the same compact surface, but the perovskite layer on the $FeCl_3$ prepared Fe_3O_3 ETL has a smaller grain size than others which may be due to the network morphology of the Fe_3O_3 film which will increase the recombination of photo-generated carriers in the grain interface. From Fig. 4b, we can see the details of the thickness of different layers where the Fe_2O_3 layer is about 20 nm represented with red color and the perovskite layer is about 600 nm represented with green color. Photoluminescence (PL) spectra (Fig. 4c) are used here to show the carrier transfer and separation performance of the perovskite/Fe_3O_3 film. A single perovskite layer on the glass substrate is presented as a black curve with a peak at 791 nm which matches the absorbance edge and bandgap of the perovskite. And with the addition of the $FeCl_3$ prepared ETL, the value decreased which means that carriers can transport from the perovskite to Fe_2O_3 layer. We found that samples with Fe_3O_4 prepared films have a higher value than a single perovskite layer which means that the Fe_3O_4 prepared ETLs do play the role of passivation layers. The ETL prepared using 10 nm Fe_3O_4 particles has the highest value, showing the best

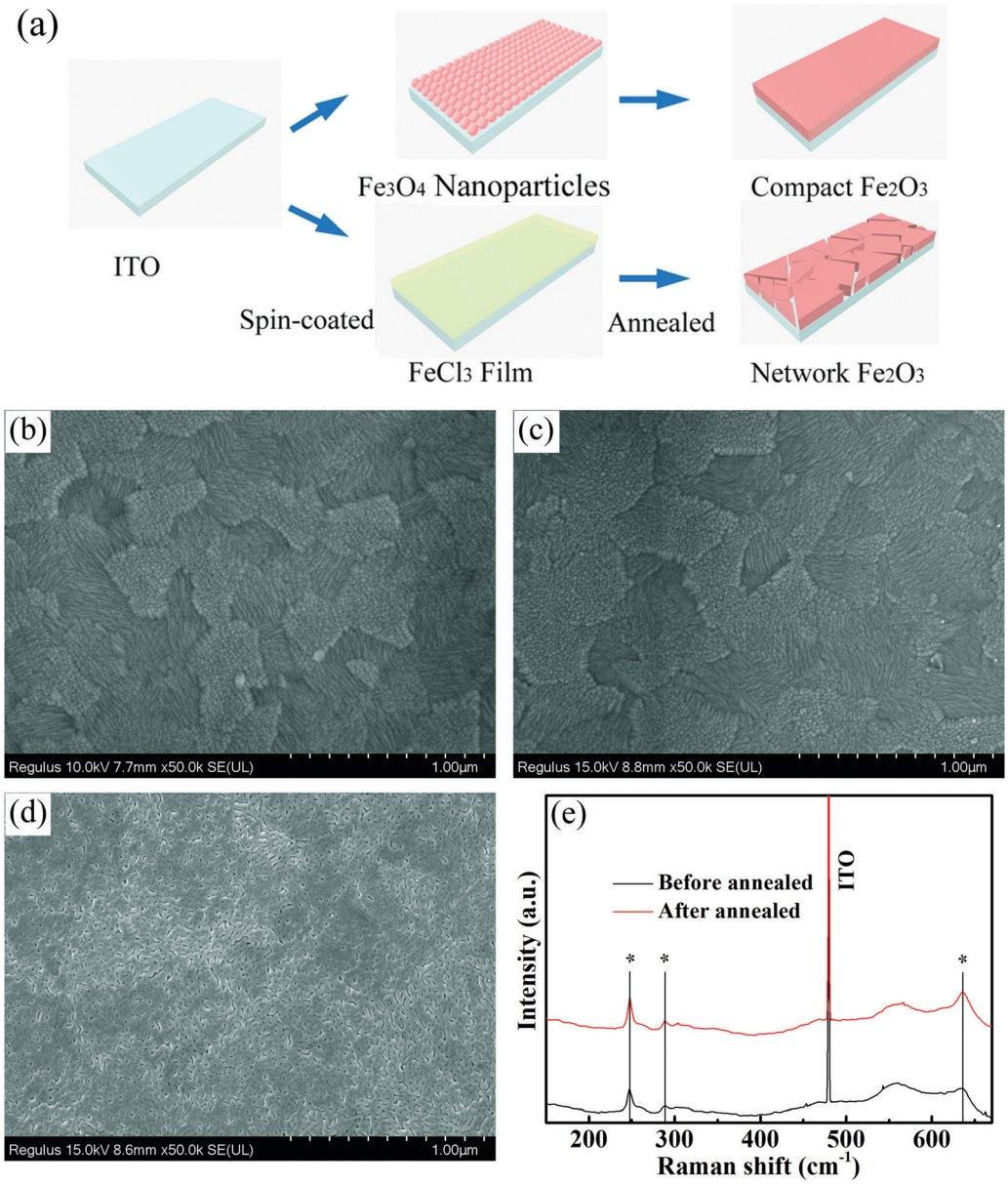

Fig. 2 (a) Schematic of Fe_2O_3 films. Top view SEM images of substrates: (b) ITO glass, (c) Fe_2O_3 prepared with 10 nm Fe_3O_4 nanoparticles and (d) Fe_2O_3 prepared with $FeCl_3$ solution. (e) Raman spectra of the Fe_2O_3 layer.

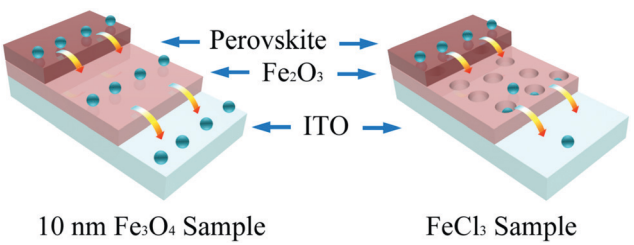

Fig. 3 Schematic of the charge transport model of different Fe_2O_3 layer based devices.

passivation ability and 5 nm and 20 nm samples have slightly lower values. This may be due to the accumulation of 5 nm nanoparticles in the spin-coating process, which may damage the properties of the ETL. However, the films prepared with 20 nm nanoparticles may overlap due to the large size of the nanoparticles, and there are some defects in the ETL. The XRD pattern of perovskite is shown in Fig. 4d, from which we can see that the peaks of the perovskite are sharp and represented with an asterisk.[44]

Current density–voltage (J–V) curves for perovskite with varieties of Fe_2O_3 films which were prepared with different Fe_3O_4 nanoparticles and $FeCl_3$ are shown in Fig. 5, and all samples are tested under AM 1.5G (from 1.2 V to 0 V, a scan step of 0.04 V and a scan rate of 100 mV s^{-1}). The photovoltaic parameters including short-current density (J_{sc}), open-voltage (V_{oc}), fill factor (FF) and PCE are shown in Table 1 and the summarized average photovoltaic parameters of 20 devices are

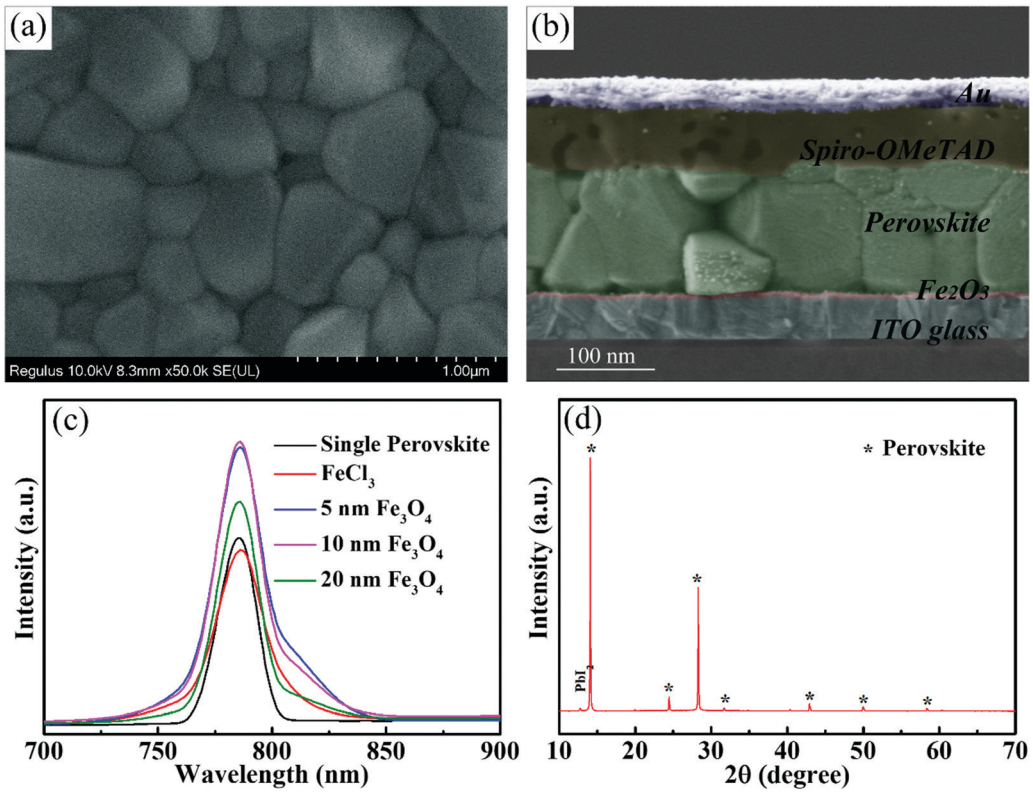

Fig. 4 (a) Top view SEM of the perovskite layer. (b) Cross sectional SEM of the solar cell. (c) PL spectra of perovskite with different substrates. (d) XRD pattern of the perovskite layer.

shown in Table S1 (ESI†). From Fig. 5a, we can see that the sample prepared with $FeCl_3$ has the lowest V_{oc}, J_{sc}, FF and PCE of 0.77 V, 23.1 mA cm^{-2}, 43.5 and 7.72%. We consider that this low performance, especially in the V_{oc} is because the Fe_2O_3 layer is not compact enough to fully play the role of an ETL. The potential difference between the quasi-Fermi levels of different ETLs may also cause different V_{oc}.[45] For the samples prepared with different Fe_3O_4 nanoparticles, the 10 nm sample shows the best performance and has the highest V_{oc} of 0.99 V, FF of 58.3 and PCE of 14.33%. This highest efficiency also reflects that 10 nm nanoparticles are the best for the Fe_2O_3 film, while the films composed of 5 nm and 20 nm nanoparticles still have some defects, which may be due to the fact that the accumulation of a small number of particles (Fig. S2, ESI†) may damage the performance of the ETLs. The incident photon-to-electron conversion efficiency (IPCE) spectrum is also used here to see the light absorption of solar cells shown in Fig. S7 (ESI†). The curve shows the absorption edge at 790 nm, which is similar to the absorbance curve of perovskite. The integrated J_{sc} calculated by the IPCE curve of 22 mA cm^{-2} is close to the tested value of the J–V curve; while considering the specular reflection of the sample, the integral current is usually less than the measured value. The devices prepared with 10 nm Fe_3O_4 nanoparticles with different concentrations, spin speeds and annealing temperatures are shown in Fig. S8 (ESI†). It could be seen from the samples annealed at different temperatures that the efficiency of solar cells is very low when Fe_3O_4 is not converted to Fe_2O_3 at low temperatures. Considering all these parameters that may affect efficiency, 10 nm Fe_3O_4 nanoparticle samples with 550 °C annealing temperature, 5000 rpm spin speed and 6 mg ml^{-1} (Fe) concentration show the best performance.

Electrochemical impedance spectroscopy (EIS) measurement was performed under AM 1.5G illumination to show the charge transport and recombination performance of different ETLs. Fig. 5b shows the Nyquist plots of different ETLs, in which the tested results are shown with symbol curves and the fitted results are shown with solid line curves. We consider the semicircle at high frequency as the transfer resistance (R_{ct}) at the transport layer/perovskite interface and the transmission line at low frequency represents the recombination impedance (R_{rec}) of solar cells. The fitted curves and values of R_{ct} and R_{rec} are summarized in the ESI† (Fig. S9 and Table S2). Due to the effective passivation of the defects on the FTO surface, the R_{ct} of the Fe_3O_4 nanoparticle film is significantly smaller than that of the sample prepared with $FeCl_3$ solution. The 10 nm sample with the best passivation effect has a R_{ct} of 131 Ω and the R_{ct} of the $FeCl_3$ prepared sample is 270 Ω. The R_{rec} of the samples prepared with Fe_3O_4 nanoparticles has a comparable value to the samples prepared with $FeCl_3$. The bigger value of R_{rec} means that it is more difficult for the recombination to occur and 10 nm samples have the highest value of 676 Ω in Fe_3O_4 nanoparticle prepared devices. $FeCl_3$, 5 nm and 20 nm samples have values of 573, 465 and 577 Ω. Also, the frequency data to

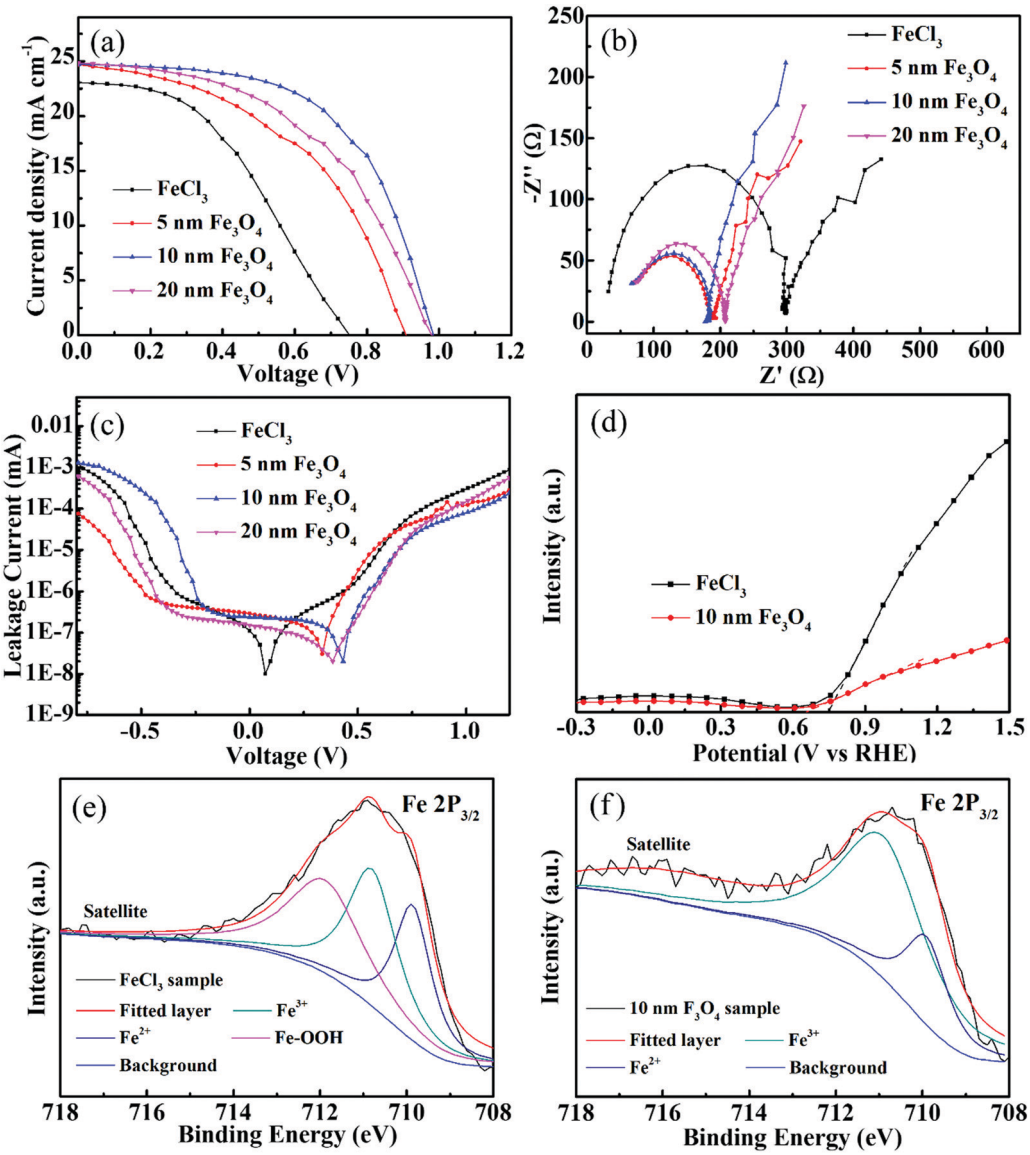

Fig. 5 (a) *J*–*V* curves, (b) Nyquist plots and (c) leakage current of perovskite solar cells with different Fe_2O_3. (d) M–S curves of $FeCl_3$ and 10 nm Fe_3O_4 nanoparticles samples. (e) and (f) XPS spectra of $FeCl_3$ and 10 nm Fe_3O_4 nanoparticle samples.

Table 1 Summary of photovoltaic parameters of solar cells with different ETLs

Sample	V_{oc} (V)	J_{sc} (mA cm^{-2})	Fill factor (%)	Efficiency (%)
$FeCl_3$	0.77	23.1	43.5	7.72
5 nm	0.92	24.83	47.83	10.95
10 nm	0.99	24.79	58.31	14.33
20 nm	0.98	24.97	49.62	12.26

the highest point of the semicircle of $FeCl_3$, 5 nm, 10 nm and 20 nm samples are 39 811, 100 000, 125 890 and 125 890 Hz which shows that the nanoparticle based samples have better transport ability than the $FeCl_3$ sample. *J*–*V* curves in the dark model are also measured to show the leakage performance of different Fe_2O_3 layers and are shown in Fig. 5c. The lowest point of the leakage curve of nanoparticle samples corresponds to the higher voltage, which indicates that these have better leakage performance than the $FeCl_3$ sample. At the same time, the sample with 10 nm nanoparticles at high potential also shows a lower leakage value than others, which indicates that it has better anti leakage ability. The Mott–Schottky (M–S) measurement was used here to further explore the band position of the Fe_2O_3 layer by different methods and is shown in Fig. 5d. The slope of the curve has a negative value, which indicates that the material tested is an n-type semiconductor. The potential value of the nanoparticle sample is 0.65 V *versus* reversible hydrogen electrode (RHE) and 0.76 V *versus* RHE of the $FeCl_3$ prepared sample. The lower value of the nanoparticle sample means that it has a higher band position than the $FeCl_3$ sample which is the same as the V_{oc} tendency by *J*–*V* measurement. X-ray photoelectron spectroscopy (XPS) was carried out to

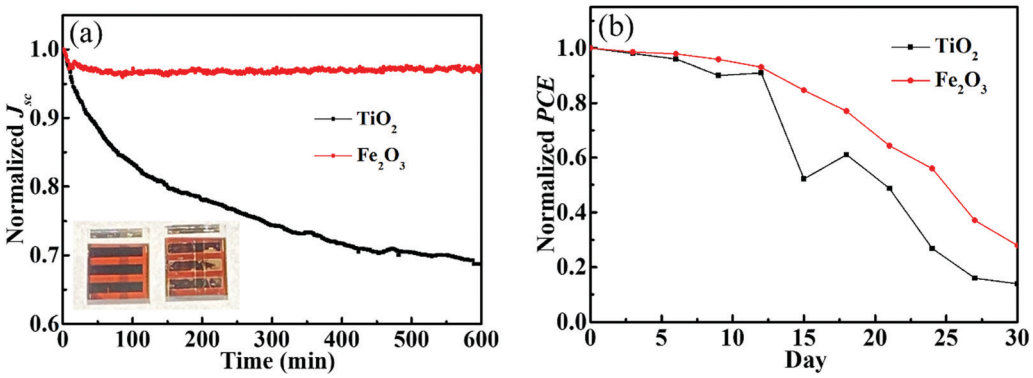

Fig. 6 (a) Maximum power point curves under a 300 W Xe lamp and (b) long time test under AM 1.5G of Fe_2O_3 and TiO_2 based solar cells.

explore the elemental states of different Fe_2O_3 samples. Fig. 5e shows the Fe $2p_{3/2}$ XPS peak of the $FeCl_3$ prepared sample, and the peak can be fitted with three curves as Fe^{3+}, Fe^{2+} and Fe–OOH. In the annealing process, $FeCl_3$ hydrolyzes to produce FeOOH and then oxidizes as much as possible to produce Fe_2O_3. At the same time, some partially oxidized Fe elements may be converted into FeO. In the XPS spectrum of the Fe_3O_4 nanoparticle prepared sample in Fig. 5f, the curve could be fitted with Fe^{3+} and Fe^{2+}. In the annealing process, most part of Fe_3O_4 was converted to Fe_2O_3 and the remaining small amount still exists in the form of divalent iron. From the XPS results, we can find that there is still some FeOOH in the $FeCl_3$ sample which may be the reason for poor charge transport. Time-resolved photoluminescence (TRPL) curves are shown in Fig. S10a (ESI†) and the fitted curves are shown in Fig. S10b (ESI†), from which we can see that the carrier lifetime values are 10.71, 22.3, 41.6 and 27.81 ns for single perovskite, 5 nm, 10 nm and 20 nm samples, respectively. This increase of carrier lifetime effectively indicates that the Fe_2O_3 film indeed acts as a passivation layer and the 10 nm sample also shows the best passivation performance. The hysteresis effect of different Fe_2O_3 layers can be calculated by $(PCE_{reverse} - PCE_{forward})/PCE_{reverse}$ and is shown in Fig. S11 (ESI†), in which the 10 nm sample shows a value of 0.3 and the $FeCl_3$ prepared sample shows a value of 0.2.

Stability is one of the most important parameters of perovskite solar cells. In order to show the stability of perovskite cells with the Fe_2O_3 layer, we prepared the cells using TiO_2 ETLs for comparison. The photovoltaic parameters of TiO_2 based solar cells are shown in Fig. S12 (ESI†). We exposed devices to a 300 W Xe lamp for continuous irradiation to obtain the results under strong ultraviolet light, and tested at the maximum power point (MPP). The curve of the Fe_2O_3 based cell in Fig. 6a has just a slightly lower which may be due to the decomposition of the perovskite during continuous exposure to the ambient atmosphere. But, for the samples prepared with TiO_2 ETLs, nearly 30% of the J_{sc} has been lost after 10 hours of irradiation. It can also be seen from the illustration that after 10 hours of irradiation, the Fe_2O_3 based cell in the left shows almost no obvious change, while the TiO_2 based sample on the right side has obvious white spots. All devices used here are prepared and measured with the same procedure, which suggests that the PCE difference mainly comes from the Fe_2O_3 and TiO_2 layer. Fig. 6b shows the long-time test of Fe_2O_3 and TiO_2 based cells which have been stored in a drying oven with less than 17% humidity and 25 °C and tested under AM 1.5G. PCEs of devices can be retained at more than 80% after two weeks and the efficiency of the Fe_2O_3 based device is still higher than that of the TiO_2 based one. The efficiency of devices using Fe_2O_3 is higher and decreases smoother than that of TiO_2 devices, which we think is due to the ultraviolet protection ability of Fe_2O_3. After 15 days of the continuous test, there was a significant decrease in the efficiency of both solar cells. We consider this may be due to the instability and etching of the silver electrode.

Conclusions

In summary, water-dispersed Fe_3O_4 nanoparticles were utilized to prepare compact and thin Fe_2O_3 film based planar Fe_2O_3 based solar cells, in which 14.3% efficiency was reached by ITO/Fe_2O_3/$(FAPbI_3)_{0.97}(MAPbBr_3)_{0.03}$/Spiro-OMeTAD/Au combination and good stability at more than 95% efficiency after 10 hours of 300 W Xe lamp irradiation was delivered. The superior performance of the as-prepared solar cells is attributed to the excellent passivation of interface defects and high UV stability by the compact nanoparticle-prepared Fe_2O_3 layer. This approach holds great promise for inexpensive, UV stable and efficient perovskite solar cells.

Author contributions

Song Fang fabricated the whole perovskite solar cells and Bo Chen prepared all Fe_3O_4 nanoparticles. Bangkai Gu and Linxing Meng commented on the manuscript. All authors wrote the manuscript and analysed the data. Hao Lu designed the whole experimental process. Hao Lu and Changming Li supervised the whole project.

Conflicts of interest

There are no conflicts to declare.

Acknowledgements

We acknowledge the support from the National Natural Science Foundation of China (51802210), the Natural Science Foundation of Jiangsu Province (BK20180970 and BK20190938), the Natural Science Foundation of the Jiangsu Higher Education Institutions of China (18KJB430023) and the Jiangsu Laboratory of Biological and Chemical Sensing and Biochip.

References

1 H. Liang, F. Wang, Z. Cheng, C. Xu, G. Li and Y. Shuai, *ES Energy Environ.*, 2020, **8**, 29–41.
2 J. P. Sawant, H. M. Pathan and R. B. Kale, *ES Energy Environ.*, 2020, **10**, 73–79.
3 S. Rakhunde, K. Gadave, D. Shinde and P. Bhujbal, *Eng. Sci.*, 2020, **12**, 117–124.
4 S. Sayyed, N. Beedri, P. Bhujbal, S. Shaikh and H. Pathan, *ES Mater. Manuf.*, 2020, **10**, 45–51.
5 R. Kapadnis, S. Bansode, A. Supekar, P. Bhujbal, S. Kale, S. Jadkar and H. Pathan, *ES Energy Environ.*, 2020, **10**, 3–12.
6 S. Satpute, J. Jagtap, P. Bhujbal, S. Sonar, P. Baviskar, S. Jadker and H. Pathan, *ES Energy Environ.*, 2020, **9**, 89–94.
7 J. Burschka, N. Pellet, S. J. Moon, R. Humphry-Baker, P. Gao, M. K. Nazeeruddin and M. Gratzel, *Nature*, 2013, **499**, 316–319.
8 H. P. Zhou, Q. Chen, G. Li, S. Luo, T. B. Song, H. S. Duan, Z. R. Hong, J. B. You, Y. S. Liu and Y. Yang, *Science*, 2014, **345**, 542–546.
9 F. Bella, G. Griffini, J.-P. Correa-Baena, G. Saracco, M. Gratzel, A. Hagfeldt, S. Turri and C. Gerbaldi, *Science*, 2016, **354**, 203–206.
10 M. Jeong, I. Choi, E. Go, Y. Cho, M. Kim, B. Lee, S. Jeong, Y. Jo, H. Choi, J. Lee, J. Bae, S. Kwak, D. Kim and C. Yang, *Science*, 2020, **369**, 1615–1620.
11 M. A. Green, A. Ho-Baillie and H. J. Snaith, *Nat. Photonics*, 2014, **8**, 506–514.
12 H. Lu, K. Deng, N. Yan, Y. Ma, B. Gu, Y. Wang and L. Li, *Sci. Bull.*, 2016, **61**, 778–786.
13 H. Lu, W. Tian, B. K. Gu, Y. Y. Zhu and L. Li, *Small*, 2017, **13**, 1701535.
14 A. Kojima, K. Teshima, Y. Shirai and T. Miyasaka, *J. Am. Chem. Soc.*, 2009, **131**, 6050–6051.
15 H. Lu, J. Zhong, C. Ji, J. Zhao, D. Li, R. Zhao, Y. Jiang, S. Fang, T. Liang, H. Li and C. M. Li, *Nano Energy*, 2020, **68**, 104336.
16 J. Yoo, G. Seo, M. Chua, T. Park, Y. Lu, F. Rotermund, Y. Kim, C. Moon, N. Jeon, J. Correa-Baena, V. Bulović, S. Shin, M. Bawendi and J. Seo, *Nature*, 2021, **590**, 587–593.
17 NREL, Research Cell Record Efficiency Chart, 2020.
18 W. Yang, D. Zhong, M. Shi, S. Qu and H. Chen, *iScience*, 2019, **22**, 534–543.
19 L. Ono, Y. Qi and S. Liu, *Joule*, 2018, **2**, 1961–1990.
20 J. Yan, W. Qiu, G. Wu, P. Heremans and H. Chen, *J. Mater. Chem. A*, 2018, **6**, 11063–11077.
21 B. Wygant, A. Ye, A. Dolocan, Q. Vu, D. Abbot and C. Mullins, *J. Am. Chem. Soc.*, 2019, **141**, 18170–18181.
22 J. Seo, H. Nishiyama, T. Yamada and K. Domen, *Angew. Chem., Int. Ed.*, 2018, **57**, 8396–8415.
23 B. Roose, J. Baena, K. Godel, M. Graetzel, A. Hagfeldt, U. Steiner and A. Abate, *Nano Energy*, 2016, **30**, 517–522.
24 M. Huang, Q. Zhao, Z. Chen, C. Shou, Q. Shen and S. Yang, *Chem. Lett.*, 2019, **48**, 700–703.
25 Y. Makimizu, J. Yoo, M. Poornajar, N. Nguyen, H. Ahn, I. Hwang, S. Kment and P. Schmuki, *J. Mater. Chem. A*, 2020, **8**, 1315–1325.
26 K. Sivula, F. L. Formal and M. Gratzel, *ChemSusChem*, 2014, **4**, 432–449.
27 C. Tang, B. Sun, M. Li, J. Zhang, X. Fan, F. Gao, Y. Tong, L. Dong and Y. Li, *J. Mater. Chem. A*, 2019, **7**, 8050–8054.
28 W. Hu, T. Liu, X. Yin, H. Liu, X. Zhao and S. Luo, *J. Mater. Chem. A*, 2017, **5**, 1434–1441.
29 J. Guo, Y. Guo, T. Liu, N. Wang, Q. Luo, H. Lin, J. Li, Q. Jiang, L. Wu and Z. Guo, *Nano Energy*, 2017, **38**, 193–200.
30 Q. Jiang, Y. Zhao, X. Zhang, X. Yang, Y. Chen, Z. Chu, Q. Ye, X. Li, Z. Yin and J. You, *Nat. Photonics*, 2019, **13**, 460–466.
31 G. Niu, S. Wang, J. Li, W. Li and L. Wang, *J. Mater. Chem. A*, 2018, **6**, 4721–4728.
32 Z. Liu, F. Cao, M. Wang, M. Wang and L. Li, *Angew. Chem., Int. Ed.*, 2020, **132**, 4190–4196.
33 J. Kim, P. Liang, S. Williams, N. Cho, C. Chueh, M. Glaz, D. Ginger and A. Jen, *Adv. Mater.*, 2015, **27**, 695–701.
34 P. Xie, Y. Liu, M. Feng, M. Niu, C. Liu, N. Wu, K. Sui, R. Patil, D. Pan, Z. Guo and R. Fan, *Adv. Compos. Hybrid Mater.*, 2021, **4**, 173–185.
35 H. Wu, Y. Zhang, R. Yin, W. Zhao, X. Li and L. Qian, *Adv. Compos. Hybrid Mater.*, 2018, **1**, 168–176.
36 H. Sun, K. Deng, Y. Zhu, M. Liao, J. Xiong, Y. Li and L. Li, *Adv. Mater.*, 2018, **30**, 1801935.
37 A. Demortiere, P. Panissod, B. P. Pichon, G. Pourroy, D. Guillon, B. Donnio and S. Begin-Colin, *Nanoscale*, 2011, **3**, 225–232.
38 H. Lu, S. Fang, J. Hu, B. Chen, R. Zhao, H. Li, C. Li and J. Ye, *ACS Omega*, 2020, **5**, 19861–19867.
39 K. Deng, Z. Liu, Y. Xin and L. Li, *Adv. Mater. Interfaces*, 2018, **5**, 1800499.
40 X. Zhang and Y. Qin, *J. Colloid Interface Sci.*, 2019, **545**, 231–241.
41 A. Lassoued, B. Dkhil, A. Gadri and S. Ammar, *Results Phys.*, 2017, **7**, 3007–3015.
42 J. Lu and C. Tsai, *Nanoscale Res. Lett.*, 2014, **9**, 230–238.
43 P. Panta and C. Bergmann, *J. Mater. Sci. Eng.*, 2015, **5**, 100217.
44 J. Wang, F. Meng, R. Li, S. Chen, X. Huang, J. Xu, X. Lin, R. Chen, H. Wu and H. Wang, *Sol. RRL*, 2020, **4**, 2000091.
45 S. Ryu, J. Noh, N. Jeon, Y. Kim, W. Yang, J. Seo and S. Seok, *Energy Environ. Sci.*, 2014, **7**, 2614–2618.